Classical density functional theory and the phase-field crystal method using a rational function to describe the two-body direct correlation function

N. Pisutha-Arnond, V. W. L. Chan, M. Iyer, V. Gavini, and K. Thornton

Phys. Rev. E **87**, 013313 — Published 30 January 2013

DOI: 10.1103/PhysRevE.87.013313

Modeling Classical Density Functional Theory and the Phase-Field Crystal Method using a Rational Function to Describe the Two-body Direct Correlation Function

N. Pisutha-Arnond,[1,*] V. W. L. Chan,[1,†] M. Iyer,[2,‡] V. Gavini,[2,§] and K. Thornton[1,¶]

[1] *Materials Science and Engineering Department, University of Michigan, Ann Arbor, Michigan, 48109, USA*

[2] *Department of Mechanical Engineering, University of Michigan, Ann Arbor, Michigan, 48109, USA*

Abstract

We introduce a new approach to represent a two-body direct correlation function (DCF) in order to alleviate the computational demand of classical density functional theory (CDFT), and enhance the predictive capability of the phase-field crystal (PFC) method. The approach utilizes a rational function fit (RFF) to approximate the two-body DCF in Fourier space. We use the RFF to show that short-wavelength contributions of the two-body DCF play an important role in determining the thermodynamic properties of materials. We further show that using the RFF to empirically parameterize the two-body DCF allows us to obtain the thermodynamic properties of solids and liquids that agree with the results of CDFT simulations with the full two-body DCF without incurring significant computational costs. In addition, the RFF can also be used to improve the representation of the two-body DCF in the PFC method. Lastly, the RFF allows for a real-space reformulation of the CDFT and PFC method, which enables descriptions of nonperiodic systems and the use of non-uniform/adaptive grids.

* nirand@umich.edu

† vicchan@umich.edu

‡ mrinal@umich.edu

§ vikramg@umich.edu

¶ kthorn@umich.edu

I. INTRODUCTION

Materials modeling is challenging due to the vast length and time scales that are involved. For example, in a study of the deformation of polycrystalline metals, atomistic resolution is required for an accurate description of dislocation energetics and dynamics; therefore, models having atomistic resolution such as molecular dynamics (MD) are suitable for simulating such processes. However, MD requires a time step small enough to resolve atomic vibrations, which limits MD simulations to very short time scales. For example, high strain rates are often used, making it difficult to perform direct comparisons with experiments [1]. On the other hand, mesoscale models, such as phase-field methods, are used extensively to study diffusive transport phenomena such as grain growth [2–6] on experimentally relevant time scales. However, the phase-field methods lack descriptions of atomistic phenomena, which limit the predictive capability of the models without additional auxiliary field variables such as those that describe grain orientations [7–12] and dislocations [13–16]. Furthermore, when the physical problem involves multiple phenomena, it becomes challenging to incorporate many auxiliary field variables in a thermodynamically self-consistent manner.

Two approaches that address these issues are classical density functional theory (CDFT) [17–19] and the phase-field crystal (PFC) method [20–22]. A common feature of these approaches is the description of a system via the free energy functional of an atomic density field that is minimized not only by a uniform field (representing liquid) but also by a periodic field (representing solid). The periodic field represents atomic arrangements, and thus it allows for an atomic-scale description of materials [20, 21, 23, 24]. The evolution of the density field can be described by dissipative dynamics [20, 25–27], which bypasses the lattice-vibration time scale and enables consideration of diffusive times scales while retaining atomistic resolution. However, the origins of these two methods are different. The CDFT is a reformulation of statistical mechanics and attempts to predict material properties by employing a correlation function that contains structural information at the atomistic scale. On the other hand, the original form of the PFC method is derived from the Swift-Hohenberg model of pattern formation [28] and is intended to provide phenomenological descriptions of material behavior. Nevertheless, the link between the CDFT and PFC method was established by Elder and co-workers [29], and the PFC method can thus be considered a simplified form of the CDFT of freezing [23], with a computational efficiency afforded by a

lower spatial-resolution requirement than that of CDFT.

While the approximation to obtain the PFC method alleviates the high computational cost of CDFT, it affects predictive capabilities of the formulation. Therefore, the goal of this work is to develop numerical techniques that increase the computational efficiency of CDFT and improve the accuracy of the PFC method. In particular, we propose a rational function fit, a ratio of polynomials, to approximate the Fourier-space two-body direct correlation function (DCF) that is typically used in the CDFT of freezing. We henceforth refer to this approach as the rational function fit (RFF) method. Additionally, the RFF method allows a real-space reformulation of the governing equations when the rational function is expressed as a summation of partial fractions, enabling the use of non-uniform/adaptive grids and descriptions of nonperiodic systems.

We use the RFF method to examine the importance of short-wavelength contributions in the two-body DCF that is used in CDFT. Our studies on iron (Fe) show that the short-wavelength contributions influence the thermodynamic properties not only quantitatively, but also qualitatively. For example, the phase stability of the face-centered-cubic (FCC) structure has a strong dependence on the short-wavelength contributions in the DCF, which is typically not accurately accounted for in PFC studies. We also show that, within the framework of the RFF method, it is possible to empirically parameterize the two-body DCF to increase computational efficiency of CDFT while retaining the accuracy of most predictions of the thermodynamic properties in comparison to those of CDFT with the full two-body DCF. We also demonstrate that the RFF can be used to improve the representation of the two-body DCF in the PFC model.

In this paper, we only focus on improving the predictive capability of CDFT and the PFC method for thermodynamic properties of a solid-liquid system such as solid-liquid interfacial free energies and solid/liquid densities at solid-liquid coexistence. We have chosen not to address mechanical properties such as bulk moduli (as in Ref. [30]) since we have recently discovered that there are inconsistencies in calculating elastic constants using the PFC method [31]. Specifically, the conventional procedure for calculating elastic constants in the PFC method is not equivalent to those defined from the theory of thermoelasticity of stressed materials [32–34]. Therefore, the applicability of the RFF to improve the prediction of mechanical properties and of mechanical phenomena (such as deformation at a finite strain rate [35, 36]) will be deferred to future investigations.

In the following, we briefly review the CDFT and PFC formulations in Sections II A and II B, respectively. We propose the RFF method in Section III. The importance of the short-wavelength contributions is examined in Section IV, and the empirical parameterization of the DCF is discussed in Section V. The RFF method is then applied to the PFC formulation in Section VI, followed by a discussion of the real-space reformulation of the RFF method in Section VII. In Section VIII, we compare Fourier-space and real-space implementations. Lastly, we conclude the paper with a summary.

II. BACKGROUND

A. Classical density function theory of freezing

Here, we provide a brief description of CDFT; for a more comprehensive discussion, we refer readers to Ref. [18]. The CDFT is a reformulation of statistical mechanics where a one-to-one correspondence exists between the equilibrium atomic one-body probability density, $\rho(\mathbf{r})$, and the external potential, $V_{ext}(\mathbf{r})$. This one-to-one correspondence enables a formulation of the intrinsic Helmholtz free energy, $\mathcal{F}\big(\rho(\mathbf{r})\big)$, which is a unique functional of $\rho(\mathbf{r})$. Furthermore, the functional derivative of $\mathcal{F}\big(\rho(\mathbf{r})\big)$ with respect to $\rho(\mathbf{r})$ gives the intrinsic chemical potential, $\psi(\mathbf{r})$:

$$\frac{\delta\mathcal{F}\big(\rho(\mathbf{r})\big)}{\delta\rho(\mathbf{r})} = \psi(\mathbf{r}) = \mu - V_{ext}(\mathbf{r}). \tag{1}$$

The intrinsic chemical potential is related to the chemical potential, μ, via

$$\mu = \psi(\mathbf{r}) + V_{ext}(\mathbf{r}). \tag{2}$$

In the absence of an external potential, which is the focus of the present work, $\psi(\mathbf{r}) = \mu$. The functional $\mathcal{F}\big(\rho(\mathbf{r})\big)$ can be written in the form:

$$\mathcal{F}\big(\rho(\mathbf{r})\big) = \mathcal{F}_{id}\big(\rho(\mathbf{r})\big) + \mathcal{F}_{ex}\big(\rho(\mathbf{r})\big)\ . \tag{3}$$

The first term on the right-hand side of the above equation corresponds to the ideal-gas contribution given by

$$\mathcal{F}_{id}\big(\rho(\mathbf{r})\big) = k_BT\int d\mathbf{r}\rho(\mathbf{r})\left(\ln[\rho(\mathbf{r})\lambda_T^3] - 1\right), \tag{4}$$

where λ_T is the de Broglie wavelength and k_B is the Boltzmann constant. The second term is an excess contribution that contains structural information of the system through the n-body DCF given by

$$c^{(n)}(\mathbf{r}_1, ..., \mathbf{r}_n; [\rho]) = -\beta \frac{\delta^n \mathcal{F}_{ex}\big(\rho(\mathbf{r})\big)}{\delta\rho(\mathbf{r}_1)...\delta\rho(\mathbf{r}_n)}, \tag{5}$$

where $\beta = 1/k_BT$. The explicit functional form of $\mathcal{F}_{ex}\big(\rho(\mathbf{r})\big)$ is not known to date, and numerous techniques have been proposed to approximate this quantity [18]. In the context of freezing, a commonly used approach is to approximate $\mathcal{F}_{ex}\big(\rho(\mathbf{r})\big)$ by a functional Taylor expansion up to second order around a uniform density, ρ_0, that corresponds to the reference liquid phase density. Combined with $\mathcal{F}_{id}\big(\rho(\mathbf{r})\big)$, the free energy expression becomes [23]

$$\begin{aligned}\beta\mathcal{F}\big(\rho(\mathbf{r})\big) = \beta\mathcal{F}(\rho_0) + \beta\mu_0 \int d\mathbf{r}\Delta\rho(\mathbf{r}) + \int d\mathbf{r}\left\{\rho(\mathbf{r})\ln\left[\frac{\rho(\mathbf{r})}{\rho_0}\right] - \Delta\rho(\mathbf{r})\right\} \\ -\frac{1}{2}\int\int d\mathbf{r}_1 d\mathbf{r}_2 \Delta\rho(\mathbf{r}_1)c^{(2)}(\mathbf{r}_1, \mathbf{r}_2; [\rho_0])\Delta\rho(\mathbf{r}_2),\end{aligned} \tag{6}$$

where μ_0 is the chemical potential of the reference state, $\Delta\rho(\mathbf{r}) = \rho(\mathbf{r}) - \rho_0$, and the function $c^{(2)}(\mathbf{r}_1, \mathbf{r}_2; [\rho_0])$ is the two-body DCF of the reference uniform density state. We note that the formation of a solid phase occurs when the equilibrium density profile is a periodic non-uniform function with symmetry corresponding to a crystal lattice.

In order to compare the above CDFT free energy functional with that of the PFC method, we introduce a dimensionless one-body density,

$$n(\mathbf{r}) = \frac{\rho(\mathbf{r}) - \rho_0}{\rho_0}, \tag{7}$$

and write the scaled dimensionless energy as

$$\begin{aligned}\Delta\tilde{\mathcal{F}}_{CDFT}\big(n(\mathbf{r})\big) = \frac{\mathcal{F}\big(\rho(\mathbf{r})\big) - \mathcal{F}(\rho_0)}{k_BT\rho_0} = \int d\mathbf{r}\left\{[1 + n(\mathbf{r})]\ln[1 + n(\mathbf{r})] - n(\mathbf{r})\right\} \\ -\frac{\rho_0}{2}\int d\mathbf{r}\int d\mathbf{r}'\left\{n(\mathbf{r})c^{(2)}(|\mathbf{r} - \mathbf{r}'|)n(\mathbf{r}')\right\},\end{aligned} \tag{8}$$

where we set the chemical potential of the reference state to be zero. It is further assumed that $c^{(2)}$ is isotropic.

The form of the two-body DCF plays an important role in determining the equilibrium density profile and, in turn, the numerical efficiency of the model. To illustrate, let us consider a two-body DCF in Fourier space, $\hat{c}^{(2)}(k)$, where k is the magnitude of the Fourier-space vector, $k = |\mathbf{k}|$. The equilibrium profile, $n(\mathbf{r})$, can be expressed as a summation of

density waves:

$$n(\mathbf{r}) = \bar{n}\left(1 + \sum_j u_j e^{i\mathbf{G}_j\cdot\mathbf{r}}\right), \tag{9}$$

where $\bar{n}$ is the average density, $\mathbf{G}_j$ is a linear combination of the primitive reciprocal lattice vectors, and u_j is the corresponding density wave amplitude. The j^{th} term in the above expansion will decrease the excess contribution to the free energy if $\hat{c}^{(2)}(|\mathbf{G}_j|)$ is positive (indicating correlation); in such a case, the density wave mode with the wave vector $\mathbf{G}_j$ is enhanced. On the other hand, the j^{th} term in the expansion above will increase the excess contribution to the free energy if $\hat{c}^{(2)}(|\mathbf{G}_j|)$ is negative (indicating anti-correlation), which would lead to suppression of the density wave mode.

Typical two-body DCFs in Fourier space have oscillations that contain positive values even at large k, which imply the presence of short-wavelength correlations in these systems. While these effects decrease with increasing k, they are nevertheless important. These short-wavelength correlations give rise to sharp peaks in the atomic probability density, which require a large number of basis functions or a very fine computational grid to attain a sufficiently accurate numerical representation. These computational limitations are alleviated in the PFC method, which is discussed below.

B. Phase-field crystal method

The PFC method was initially developed as a reformulation of the Swift-Hohenberg model of pattern formation [28]. However, the connection between Eq. (8) and the free energy functional of the PFC method was later established by Elder and co-workers [29] through approximations to the CDFT free energy. First, the ideal contribution in Eq. (8) is approximated by its Taylor expansion:

$$(1+n(\mathbf{r}))\ln(1+n(\mathbf{r})) - n(\mathbf{r}) \approx \frac{1}{2}n(\mathbf{r})^2 - \frac{a_t}{6}n(\mathbf{r})^3 + \frac{b_t}{12}n(\mathbf{r})^4 \ , \tag{10}$$

with $a_t = b_t = 1$ in the original formulation of the PFC method. However, in later works [30], a_t and b_t have been used as empirical parameters to fit specific properties of liquid and solid. The second approximation constitutes a fourth-order fit (4P) of the two-body DCF in Fourier space as

$$\hat{C}^{(2)}_{4P}(k) \equiv \rho_0 \hat{c}^{(2)}_{4P}(k) = \mathcal{C}_0 + \mathcal{C}_2 k^2 + \mathcal{C}_4 k^4 \ , \tag{11}$$

where the constants $\mathcal{C}_0$, $\mathcal{C}_2$, and $\mathcal{C}_4$ are fitting coefficients. These approximations yield the PFC free energy functional of the form:

$$\Delta\tilde{\mathcal{F}}_{4P}\big(n(\mathbf{r})\big) = \int d\mathbf{r}\left[n(\mathbf{r})\frac{1-\mathcal{C}_0+\mathcal{C}_2\nabla^2-\mathcal{C}_4\nabla^4}{2}n(\mathbf{r}) - \frac{a_t}{6}n(\mathbf{r})^3 + \frac{b_t}{12}n(\mathbf{r})^4\right]. \quad (12)$$

Recently, an expansion up to the eighth order was proposed in order to better approximate the two-body DCF [30]:

$$\hat{C}^{(2)}_{8P}(k) \equiv \rho_0\hat{c}^{(2)}_{8P}(k) = \mathcal{C}_m - \Gamma\left(\frac{k_m^2-k^2}{k_m^2}\right)^2 - E_B\left(\frac{k_m^2-k^2}{k_m^2}\right)^4, \quad (13)$$

where

$$\Gamma = -\frac{k_m^2\mathcal{C}_c}{8}, \quad E_B = \mathcal{C}_m - \mathcal{C}_0 - \Gamma, \quad (14)$$

and k_m, $\mathcal{C}_0$, $\mathcal{C}_m$, and $\mathcal{C}_c$ are fitting constants. We denote this approximation as the eighth-order fit (8P). The corresponding free energy is

$$\Delta\tilde{\mathcal{F}}_{8P}\big(n(\mathbf{r})\big) = \int d\mathbf{r}\left[\frac{n(\mathbf{r})}{2}\left(1-\mathcal{C}_m+\Gamma\left(\frac{k_m^2+\nabla^2}{k_m^2}\right)^2 + E_B\left(\frac{k_m^2+\nabla^2}{k_m^2}\right)^4\right)n(\mathbf{r}) - \frac{a_t}{6}n(\mathbf{r})^3 + \frac{b_t}{12}n(\mathbf{r})^4\right]. \quad (15)$$

The fitting parameters in Eqs. (11) and (13) are chosen so that these fits accurately describe the two-body DCF up to the first peak [30, 37], and are employed in the present work. Compared to the 4P, the 8P in Eq. (13) provides an additional fitting parameter to better fit the DCF. Beyond the first peak, the values of the fits for both 4P and 8P become increasingly negative as k increases. These large anti-correlations at short wavelengths results in the high-frequency density waves being energetically unfavorable, thus resulting in nonlocalized, smooth equilibrium density profiles and in turn improved computational efficiency.

The dynamics of the PFC method is given by:

$$\frac{\partial n(\mathbf{r},\tau)}{\partial\tau} = \nabla^2\frac{\delta\Delta\tilde{\mathcal{F}}_{PFC}[n(\mathbf{r},\tau)]}{\delta n(\mathbf{r},\tau)}, \quad (16)$$

where the subscript PFC denotes the free energy given in Eq. (12) or Eq. (15). This equation can be obtained from mass conservation where the flux is driven by the gradient of the chemical potential [20], which is a variational derivative of the free energy with respect to the atomic density.

A polynomial approximation of the two-body DCF is limited in the ability to represent the DCF accurately beyond the first peak. In order to improve the predictive capability of the PFC method relative to CDFT, it may be important to consider the short-wavelength correlations beyond the first peak. To this end, we propose an alternative method for representing the two-body DCF using a ratio of polynomials in the next section. We subsequently demonstrate that such an approach addresses the limitation in the predictive capability of the PFC method and the computational demand of CDFT, as well as enables a real-space reformulation of these methods.

III. RATIONAL FUNCTION FIT

In order to address the aforementioned issues, we introduce a new method in which a rational function—a ratio of polynomials—is used to fit the two-body DCF in Fourier space. The resulting rational function can be decomposed into a summation of partial fractions as

$$\hat{C}^{(2)}_{RFF}(k) \equiv \rho_0 \hat{c}^{(2)}_{RFF}(k) = \sum_j \left[\frac{A_j}{k^2 + \alpha_j} + \frac{A_j^*}{k^2 + \alpha_j^*} \right], \tag{17}$$

where A_j and α_j are fitting coefficients which are generally complex numbers and the asterisk denotes a complex conjugate. We refer to this approach as the rational function fit (RFF) method, and denote mT-RFF as the rational function fit comprising of m partial fraction terms. The above fit accurately captures the oscillatory behavior of the two-body DCF and satisfies the short-wavelength limit, i.e., $\hat{C}^{(2)}_{RFF}(k) = 0$ as $k \to \infty$. The coefficients A_j and α_j can be determined from curve fitting algorithms, and we use the Curve Fitting Toolbox (version 2.2) in the Matlab software (version 7.10.0.499) in the present work. We find that odd numbers of partial fractions, which results in one pair of coefficients, A_j and α_j, being real values, are better suited for the given problem. Therefore, we present only these cases.

In Sections IV, V and VI, we demonstrate how the RFF can be used to address the issues of high computational cost in CDFT and limited predictive capability of the PFC method. To this end, we consider the two-body DCF of Fe, which is shown as a solid line in Fig. 1. This data, provided by Wu [38], was obtained from embedded-atom-method molecular dynamics (EAM-MD) simulations described in Ref. [39]. We will subsequently denote this data as $\hat{c}^{(2)}_{MD}(k)$, or $\hat{C}^{(2)}_{MD}(k) \equiv \rho_0 \hat{c}^{(2)}_{MD}(k)$. This data was obtained from a simulation at a temperature of $T = 1772$ K and a density of $\rho_0 = 0.0801$ $\mathring{A}^{-3}$, which is used as the reference

density for normalizing the governing equations. Since MD simulations cannot provide the long-wavelength limit of the two-body DCF due to the restricted size of simulation domains, this limit was approximated from experimental data to be $\hat{C}^{(2)}_{MD}(0) \approx -49$ [30].

IV. EXAMINING THE ROLE OF SHORT-WAVELENGTH CONTRIBUTIONS OF THE TWO-BODY DIRECT CORRELATION FUNCTION

In this section, we examine the importance of the short-wavelength contributions in the two-body DCF to the thermodynamic properties computed using CDFT. We employ the RFF method that enables us to systematically control the short-wavelength contributions. We first describe various fits of $\hat{C}^{(2)}_{MD}(k)$ employed in this work followed by the procedure used to calculate the relevant thermodynamic quantities. We subsequently present the results of the calculations and discuss our findings.

A. The rational function fits of the two-body direct correlation function of Fe

We show the various fits of $\hat{C}^{(2)}_{MD}(k)$ using the RFFs in Figs. 1(a) and 1(b). Figure 1(a) shows that all 4 RFFs satisfy the following two limits: $\hat{C}^{(2)}_{RFF}(0) = -49$ and $\hat{C}^{(2)}_{RFF}(\infty) \to 0$. The difference between these 4 RFFs is the number of the partial fraction terms in the RFF, which determines the number of peaks of $\hat{C}^{(2)}_{MD}(k)$ that are captured (see Fig. 1(b)). The 3-term RFF (the RFF that can be decomposed into three partial fraction terms), denoted by 3R, captures $\hat{C}^{(2)}_{MD}(k)$ accurately up to the first peak, while the 5R captures up to the second peak. The 7R and 9R capture up to the third and fourth peaks, respectively. In this manner, we systematically improve the accuracy of the representation of the short-wavelength contributions in the two-body DCF, making it possible to study their effect on the thermodynamic properties.

In Fig. 1(c), we show the plots of the 8P and 4P, whose coefficients are chosen to describe $\hat{C}^{(2)}_{MD}(k)$ up to its first peak [30, 37]. Both fits become increasingly negative beyond the first peak, approaching negative infinity as $k \to \infty$. We further note that an additional fitting parameter in the 8P (compared with that of the 4P) allows the 8P to capture the desired long-wavelength limit, $\hat{C}^{(2)}_{8P}(0) = -49$, whereas the 4P does not. To make consistent comparisons with RFF results, we will only use the thermodynamic properties computed

from using the 8P of $\hat{C}^{(2)}_{MD}(k)$.

B. Procedures to calculate solid-liquid properties

We consider the following thermodynamic properties: phase stability of body-centered-cubic (BCC) and face-centered-cubic (FCC) solids; solid-liquid coexisting densities; and solid-liquid interfacial free energies. These properties are obtained from analyzing equilibrium free energies of bulk solid, bulk liquid, and coexisting solid-liquid phase. The free energy of the bulk liquid can be calculated analytically due to the uniformity of the bulk liquid-density profile, while the free energies of the other systems are obtained from numerical calculations of the equilibrium density profiles.

We use two methods to determine the equilibrium density profile. The first method is a numerical relaxation based on a globally conserved dynamics [40], also known as the conserved Allen-Cahn dynamics:

$$\frac{\partial n(\mathbf{r},\tau)}{\partial \tau} = -\frac{\delta \Delta\tilde{\mathcal{F}}_{CDFT}\big(n(\mathbf{r},\tau)\big)}{\delta n(\mathbf{r},\tau)} + \frac{1}{V}\int d\mathbf{r}\frac{\delta \Delta\tilde{\mathcal{F}}_{CDFT}\big(n(\mathbf{r},\tau)\big)}{\delta n(\mathbf{r},\tau)}, \tag{18}$$

where V is the volume of the system. This method is used in all cases except for the calculations of the phase stability of the FCC solid. The second method is a semi-analytical method where we approximate the equilibrium density profile constructed from non-overlapping Gaussian functions centered at the lattice sites. We then minimize the free energy with respect to parameters that control the Gaussian peak height/width and unit-cell size. The details of the Gaussian approximation are discussed in Appendix A. This relaxation method is employed for the FCC solid as the density profiles are sharply peaked around the lattice sites, making full numerical relaxation too expensive.

Following the procedure in Ref. [30], we determine the solid-liquid coexisting region from a common-tangent construction of the free energy density curves [41]. The solid-liquid interfacial free energy, γ, is evaluated by constructing a long slab whose size is one unit-cell in the plane of the interface and 64 unit-cell long in the direction perpendicular to the interface. One half of the slab is initialized as the bulk solid at the solid density at solid-liquid coexistence and the other half is initialized as the bulk liquid at the liquid density at the solid-liquid coexistence. The slab is then relaxed numerically using Eq. (18) with periodic boundary conditions, and γ is calculated by subtracting out free energies of the

bulk phases.

C. Results and discussions

The resulting thermodynamic properties from the CDFT simulations with the different fits to $\hat{C}^{(2)}_{MD}(k)$ are shown in Table II. Figure 2 shows the free energy density curves of the liquid and the BCC solids, which are used to calculate the densities at the solid-liquid coexistence and volume expansion during melting. The integrated density profiles per unit area along the direction normal to (110) plane are shown in Fig. 3 and the density profiles on the (100) crystal plane of the BCC solids at the solid-liquid coexistence are shown in Fig. 4.

Table II also shows the stability of the FCC solid (bottom row) from the simulations using the RFFs and 8P. The stable behavior (denoted by "S" in Table II) of the FCC solid is shown in Fig. 5(a) for the $\hat{C}^{(2)}_{MD}(k)$ CDFT simulation, where the FCC solid attains stability at large densities. This behavior is captured by the 7R and 9R CDFT simulations (see Figs. 5(c) and 5(b), respectively). However, the 5R CDFT simulation shows a metastable behavior (denoted by "MS" in Table II) of the FCC phase, where the FCC phase has energy minima that are higher than the energy minima of the BCC phase. This metastable behavior can be seen from the free energy curves of the FCC and BCC solids shown in Fig. 5(d). We further note that the FCC phase is not stable (denoted by "NS" in Table II) for the 3R and 8P of the two-body DCF.

Comparing results from the 3R CDFT simulations with those of the 8P, we do not find a significant difference in the solid and liquid properties as well as in the density profiles. We note that these two fits capture the correlations accurately up to the first peak in the two-body DCF, but do not account for the shorter wavelength correlations. The more accurate asymptotic behavior of the 3R does not substantially improve the accuracy of the computed thermodynamic properties in comparison to the 8P. However, the 5R to 9R CDFT simulations show progressively improved accuracies in the predictions (see Table II), with the most significant improvement between the 3R and 5R. We note that the 5R accurately represents the correlations up to the second peak in the two-body DCF. Further, the 7R and 9R accurately represent the correlations up to the third and fourth peaks, respectively. Although the accuracy of the thermodynamic properties improves between the 7R and 9R,

the extent of the improvement is not as significant as that seen between the 3R to 5R, and the 5R to 7R. We attribute this observation to the fact that the amplitude of the correlations in the two-body DCF asymptotically decays, and therefore the role of increasingly shorter wavelength correlations to the thermodynamic properties is progressively less significant. Nevertheless, the 5R does not predict the stability of the FCC phase, suggesting that the correlations up to the third peak in the two-body DCF appear to be important for phase stability. Finally, by noting that the prediction of the 3R does not significantly differ from that of the 8P, we believe that the thermodynamic properties are relatively insensitive to the anti-correlations beyond the first peak.

In this section, the short-wavelength correlations are shown to be important even for a qualitative prediction of thermodynamic properties. Therefore, the computational demand of CDFT, arising from the sharp localized peaks in the density profiles, cannot be alleviated by simply suppressing the short-wavelength correlations (as done in most PFC methods) without sacrificing the predictive capability of the model considerably. We now propose an empirical parameterization of the two-body DCF as a RFF, which seeks to improve the predictive capability using fewer terms in the RFF.

V. EMPIRICAL PARAMETRIZATION OF THE TWO-BODY DIRECT CORRELATION FUNCTION

As seen in the previous study, there is a significant improvement in the accuracy of the predicted thermodynamic properties upon resolving the second peak in the two-body DCF (as seen in the differences between the 3R and 5R CDFT results). Thus, we seek to construct a parameterization of the two-body DCF that yields the accurate thermodynamic properties of the liquid and solid phases, while providing smoother atomic density profiles, by using a RFF that represents the correlations up to the second peak. We begin with the 5R and systematically vary the value of the function at both peaks, keeping the curvature values and the locations of the peaks similar to those from $\hat{C}^{(2)}_{MD}(k)$. The locations of the peaks are fixed to maintain the lattice constants of the solid crystal, and the curvature values of the peaks are held constant to retain the interfacial properties of the liquid-solid interface, as suggested by Ref. [39].

In terms of implementation, an analytical expression of the modified 5R, M5R, is manually

constructed from a spline interpolation of discrete data points. We then employ the semi-analytical method to determine the fit that yields similar solid free energies to the simulations using $\hat{C}^{(2)}_{MD}$ at the solid density at the solid-liquid coexistence; this procedure allows us to quickly experiment with a large number of fits. Subsequently, we fit the data with the RFF and use the numerical method to verify the fit.

The M5R, shown in Fig. 6(a), is similar to the 5R except for a slightly higher value of the function at the second peak. The corresponding free energy of the BCC solid from the M5R CDFT simulations, shown in Fig. 6(b), is in good agreement with those of $\hat{C}^{(2)}_{MD}(k)$. The slightly higher value at the second peak results in the density profile from the M5R CDFT simulations being more localized than those from the 5R. This is apparent from the higher amplitudes of density peaks at the BCC lattice sites shown in Fig. 4, and from the integrated density profile per unit area shown in Fig. 3. The liquid and solid properties of the BCC phase from the M5R CDFT simulations are tabulated in Table III, and are in good agreement with the results from the CDFT simulations using $\hat{C}^{(2)}_{MD}(k)$. Further, we note that most of the thermodynamic properties computed from the M5R CDFT simulations are more accurate than those computed from the 9R. However, the stability of the FCC phase is not predicted by the M5R, further emphasizing the role of correlations corresponding to the third peak in determining the FCC phase stability of Fe.

As demonstrated from the results, the M5R predicts most thermodynamic properties with greater accuracy than the 9R. As seen in Fig. 4, the density profiles from the M5R CDFT simulations are considerably smoother than those of the 9R, which leads to the improved computational efficiency of the CDFT simulations.

VI. APPLICATION OF RFF TO THE PFC METHOD

As discussed in Section II B, it has been shown that the PFC method can be derived from the CDFT of freezing by two approximations [29]: (i) a fourth-order polynomial approximation of the ideal contribution; (ii) a polynomial approximation to the two-body DCF in Fourier space. To date, the polynomial approximations of the two-body DCF in the PFC formulations have at most considered resolving the first two peaks [42]. It has been demonstrated in Sections IV and V that the RFF method can be used to accurately describe the two-body DCF up to the fourth peak, and possibly beyond. Thus, we seek to apply the

RFF to the PFC method to enhance its predictive capability.

It is important to note that the RFF cannot be directly used in the PFC free energy functional because the evolution equation can potentially yield a discontinuous density profile as shown in Fig. 7(b). The reason for this is demonstrated by considering the approximation of the ideal contribution in Eq. (10). For instance, by taking $a_t = 0.6917$ and $b_t = 0.0854$ from Ref. [30], the approximation of the ideal contribution yields a double-well function as opposed to a single-well function, as shown in Fig. 7(a). This double-well behavior energetically favors the value of $n(\mathbf{r})$ to be separated into values corresponding to the densities associated with the minima, and potentially leads to a discontinuous profile. In the PFC formulations such as those using the 4P and the 8P, the large anti-correlations at short-wavelengths in these fits prevent such discontinuity from forming. The asymptotic behavior of the RFFs at large k, on the other hand, does not pose sufficient energy penalty to prevent such discontinuity from forming. To illustrate this, we use the approximation to the ideal contribution in Eq. (10) along with the 3R, and evolve the density profile using the equilibrium density from the 3R CDFT simulation as the initial condition. After a few iterations, the resulting density profile yields discontinuities as shown in Fig. 7(b). The values of $n(\mathbf{r})$ at the peaks and troughs are around 0 and 9, which are close to the densities corresponding to the minima of the double-well function in Fig. 7(a).

In order to circumvent this issue, we propose an approximation to the two-body DCF of the following form:

$$\hat{C}^{(2)}_{RP}(k) = \sum_{j=1} \left[\frac{A_j}{k^2 + \alpha_j} + \frac{A_j^*}{k^2 + \alpha_j^*} \right] + \sum_{l=0}^{p} \mathcal{C}_l k^{2l} \,, \tag{19}$$

where the subscript RP denotes the combined RFF and polynomial fit, and A_j, α_j and $\mathcal{C}_l$ are fitting coefficients. By setting $\mathcal{C}_p$ (the coefficient of the highest-order polynomial term) to be negative, we can control $\hat{C}^{(2)}_{RP}(k)$ to approach negative infinity as $k \to \infty$, thus increasing the energy penalty for short-wavelength density waves. Figure 8 shows the resulting fits using 3, 5, and 7 partial-fraction terms, respectively. For each number of partial-fraction terms, we consider $p = 1$ and $p = 2$, which corresponds to including polynomial terms up to second and fourth order, respectively.

Jaatinen and coworkers have shown that the PFC free energy can predict a stable BCC phase of Fe whose properties are in agreement with those from experiments and MD simulations [30]. This is achieved by fitting the 8P to $\hat{C}^{(2)}_{MD}(k)$ so that the fit matches the

value of $\hat{C}^{(2)}_{MD}(0)$, the k-value of the first peak, k_m, and the curvature at the first peak, $d^2/dk^2\left[\hat{C}^{(2)}_{MD}(k_m)\right]$, as shown in Fig. 1(c). We demonstrate that the combined RFF and polynomial fit can capture similar features of $\hat{C}^{(2)}_{MD}(k)$ by using three terms in RFF and including up to the second-order polynomial term ($p = 1$). The resulting fit is shown in Fig. 9(a) where our fit is termed 3R2P. The 3R2P fit is almost identical to the 8P up to the first peak and begins to deviate from the 8P for higher k. Nevertheless, we show in Table I that the 3R2P fit captures almost the same features of the $\hat{C}^{(2)}_{MD}(k)$ as the 8P does. By using $a_t = 0.6917$ and $b_t = 0.0854$ for the ideal contribution in PFC, the resulting equilibrium BCC density profile from the 3R2P fit at $\bar{n} = 0.1$ is shown in Fig. 9(b). This density profile is very similar to the equilibrium density profile from the 8P at the same density (see Figs. 9(c) and 9(d)).

VII. REAL-SPACE IMPLEMENTATION

In this section, we discuss numerical techniques for evaluating the convolution integral from Eq. (8) in real space. The partial fraction decomposition allows the convolution integral to be evaluated by solving a set of inhomogeneous Helmholtz equations. The convolution integral in consideration is in the following form:

$$\mathcal{I}_c(\mathbf{r}) = \int C^{(2)}(|\mathbf{r} - \mathbf{r}'|)n(\mathbf{r}')d\mathbf{r}'. \tag{20}$$

Using $C^{(2)}_{RFF}(|\mathbf{r} - \mathbf{r}'|)$, we can rewrite the convolution integral as

$$\mathcal{I}_c(\mathbf{r}) = \sum_j \left[L_j(\mathbf{r}) + L^*_j(\mathbf{r})\right] \ , \tag{21}$$

where L_j and L^*_j can be obtained from solving the inhomogeneous Helmholtz equations:

$$\begin{aligned} -\nabla^2 L_j(\mathbf{r}) + \alpha_j L_j(\mathbf{r}) &= A_j n(\mathbf{r}) \\ -\nabla^2 L^*_j(\mathbf{r}) + \alpha^*_j L^*_j(\mathbf{r}) &= A^*_j n(\mathbf{r}) \ . \end{aligned} \tag{22}$$

We note that $L_j(\mathbf{r})$ and $L^*_j(\mathbf{r})$ can also be computed from the following integral equations:

$$\begin{aligned} L_j(\mathbf{r}) &= A_j \int \left(\frac{e^{-\sqrt{\alpha_j}|\mathbf{r}-\mathbf{r}'|}}{4\pi|\mathbf{r} - \mathbf{r}'|}\right) n(\mathbf{r}')d\mathbf{r}' \\ L^*_j(\mathbf{r}) &= A^*_j \int \left(\frac{e^{-\sqrt{\alpha^*_j}|\mathbf{r}-\mathbf{r}'|}}{4\pi|\mathbf{r} - \mathbf{r}'|}\right) n(\mathbf{r}')d\mathbf{r}', \end{aligned} \tag{23}$$

where the kernels are the three-dimensional Green's functions of the Helmholtz equation. The free energy in Eq. (8) becomes

$$\Delta\tilde{\mathcal{F}}_{CDFT}\big(n(\mathbf{r})\big) = \int d\mathbf{r}\,\{[1+n(\mathbf{r})]\ln[1+n(\mathbf{r})] - n(\mathbf{r})\} - \frac{1}{2}\int d\mathbf{r}\left\{n(\mathbf{r})\sum_j \big[L_j(\mathbf{r}) + L_j^*(\mathbf{r})\big]\right\} \tag{24}$$

and the same approach can be used to compute the PFC free energy that employs $C^{(2)}_{RP}(|\mathbf{r}-\mathbf{r}'|)$. The free energy in the above form provides a real-space formulation of the CDFT and PFC method, where the quantities $L_j(\mathbf{r})$ and $L_j^*(\mathbf{r})$ can be evaluated by direct methods such as LU factorization [43] or Krylov [44, 45] and classical pointwise iterative methods [46]. For direct solves, efficient parallel direct-solver libraries are widely available (MUMPS [47, 48], PARDISO [49, 50], SuperLU [51]) and are much faster than iterative methods when the factorization matrices of the discretization matrix can be stored and reused. However, the storage requirement rapidly increases with problem size, which becomes a limitation for large three-dimensional simulations. Iterative solvers, on the other hand, do not require the storage of the entire matrix and, therefore, are more suitable for large-scale simulations. However, we note that the discretization matrix of the Helmholtz equations in Eq. (22) are indefinite when the real part of α_j is negative. As a result, the computation of $L_j(\mathbf{r})$ and $L_j^*(\mathbf{r})$ using the iterative methods requires special treatments [52]. Many efforts over the past few decades have been devoted to the development of numerically efficient solvers for the Helmholtz equation that leads to an indefinite matrix, and we refer to a recent review article [53] and the references therein for a comprehensive overview of this field.

In this work, we use a point-wise iterative method to demonstrate our real-space formulation. We employ a two-step complex iterative Jacobi (CIJ) method [54] to solve the indefinite Helmholtz equation. When the discretization matrix of the Helmholtz equation is not indefinite [55], a standard iterative Jacobi (SIJ) method [46] is used. We note that the CIJ/SIJ method is chosen for its low memory requirement and simplicity in parallelization. Better convergence speeds are expected from more advanced methods such as the generalized minimal residual (GMRES) method [56] with appropriate preconditioners [52].

We compute the free energy densities of the BCC solid from the M5R CDFT simulations using the CIJ/SIJ methods at different grid spacings: $\Delta h = a_{BCC}/16$, $a_{BCC}/32$, $a_{BCC}/64$, and $a_{BCC}/128$, where $a_{BCC}(= 2.95)$ is the normalized lattice spacing of the BCC solid. We then compare the results with the solid free energy density from the simulation using the

Fourier spectral method at a smaller grid spacing of $\Delta h = a_{BCC}/256$, for which numerical convergence has been verified. The results are shown in Fig. 10(a) where the difference (as a measure of the numerical error) reduces as the grid spacing becomes smaller. In addition, we use the CIJ/SIJ method to simulate the interface between the liquid and BCC solid of the M5R CDFT simulation, as shown in Fig. 10(b).

VIII. COMPARISON OF FOURIER-SPACE AND REAL-SPACE IMPLEMENTATIONS

In this section, we compare the Fourier spectral method and real-space methods (CIJ/SIJ and LU factorization methods) for evaluating the convolution integral in Eq. (20). In a situation where the density profile is relatively uniform and the periodic boundary conditions are appropriate, the Fourier spectral method is a method of choice due to two advantages. First, the Fourier transform of the convolution integral in Eq. (20) can be written explicitly as

$$\hat{\mathcal{I}}_c(\mathbf{k}) = \hat{C}^{(2)}(|\mathbf{k}|)\hat{n}(\mathbf{k}), \tag{25}$$

where $\hat{n}(\mathbf{k})$ is the Fourier transforms of $n(\mathbf{r})$. Thus, the calculation of $\mathcal{I}_c(\mathbf{r})$ involves only simple pointwise operations (multiplication) and the Fourier transform operations, which can be efficiently performed by a fast Fourier transform (FFT). Examples of open-source and commercial libraries/packages for FFT are FFTW [57] (employed in this work), IBM PESSL [58] and, more recently, P3DFFT [59]. To illustrate the advantage resulting from the expression in Eq. (25), we evaluate the convolution integral in Eq. (20) where the two-body DCF is 5R and density profile is the equilibrium BCC-solid density profile from the 5R CDFT simulation (an average scaled density of 0.18) with the size of 32^3 grid points. The calculation using the Fourier spectral method took 4.6×10^{-3} s whereas the calculations using the CIJ/SIJ and direct-solve methods using the MUMPS library took 2.9 s and 0.6 s, respectively (see also a footnote [60]), all of which are performed on two Quad-Core AMD Opteron 2356 Processors, with a total of eight processors.

The second advantage is that the Fourier spectral method allows for easy implementation of an implicit time stepping scheme in numerical integration. We note that there are other more sophisticated numerical algorithms developed for evolving PFC equations (see, for

example, Refs. [61–65]). However, we consider the backward Euler time stepping scheme for simplicity. The backward Euler time stepping scheme can be written as

$$\hat{n}_{u+1}(\mathbf{k}) = \frac{1}{1+\Delta\tau|\mathbf{k}|^2(1-\hat{C}^{(2)}(|\mathbf{k}|))}\left[\hat{n}_u(\mathbf{k}) - \Delta\tau|\mathbf{k}|^2\left(-\frac{a_t}{2}\mathcal{F}^T\left[n_u^2\right] + \frac{b_t}{3}\mathcal{F}^T\left[n_u^3\right]\right)\right], \tag{26}$$

where $\Delta\tau$ is the time step size, u and $u+1$ denote the current and next time steps, and $\mathcal{F}^T$ denotes the Fourier transform operation. Here, the nonlinear terms, n^2 and n^3, are treated explicitly; i.e., they are evaluated at the time u, not $u+1$.

As an example, we calculate the maximum time step using the the backward Euler time stepping scheme for 8P and 3R2P. The maximum time step is determined by a convergence test where the convergence values, V_w and V_n, for the energy and the density profile, respectively, are defined by

$$V_w = \sqrt{\frac{\left\langle(\tilde{w}_s - \tilde{w}_r)^2\right\rangle}{\left\langle(\tilde{w}_r - \langle\tilde{w}_r\rangle)^2\right\rangle}} \times 100, \tag{27}$$

and

$$V_n = \sqrt{\frac{\left\langle(n_s - n_r)^2\right\rangle}{\left\langle(n_r - \langle n_r\rangle)^2\right\rangle}} \times 100, \tag{28}$$

where the subscript s denotes the quantity calculated from the simulation using $\Delta\tau = s$ and the subscript r denotes the reference quantity which is taken to be that calculated using $\Delta\tau = 10^{-7}$. The notation $\langle x\rangle$ denotes the arithmetic mean of x and the quantity $\tilde{w} \equiv \tilde{w}(\tilde{\mathbf{r}})$ is the position-dependent scaled energy density:

$$\tilde{w}(\tilde{\mathbf{r}}) = \frac{1}{2}n(\tilde{\mathbf{r}})^2 - \frac{a_t}{6}n(\tilde{\mathbf{r}})^3 + \frac{b_t}{12}n(\tilde{\mathbf{r}})^4 - \frac{n(\tilde{\mathbf{r}})}{2}\int C^{(2)}(|\tilde{\mathbf{r}} - \tilde{\mathbf{r}}'|)n(\tilde{\mathbf{r}}')d\tilde{\mathbf{r}}', \tag{29}$$

where $\tilde{\mathbf{r}}$ and $\tilde{\mathbf{r}}'$ denote the scaled spatial coordinates. The initial density profile is the equilibrium BCC-solid density profile from the 5R CDFT simulations (size of 32^3 grid points) as shown in Fig. 4(d) and the simulation parameters are given by $a_t = 0.6917$, $b_t = 0.0854$, and the grid spacing of 0.093. We calculate the convergence values at $\tau = 0.2$ and tabulate the results in Table IV. For the convergence values less than 0.01%, the largest time step sizes are on the order of 10^{-4}.

However, when the density profile is nonperiodic and/or highly non-uniform, a real-space implementation can be advantageous. First, the real-space formulation allows reduction of the degrees of freedom through the use of adaptive mesh refinement (AMR) in finite

element methods and finite difference methods. AMR can be useful in a situation where a portion of the domain is liquid, which is represented by a uniform density, as in the early stage of solidification, as well as in CDFT simulations in which the density is highly concentrated only near the lattice positions and is nearly uniform elsewhere. In such cases, a finely spaced mesh can be placed where the atomic density changes rapidly, while a coarser mesh can be used elsewhere. Therefore, we expect that the adaptivity of the mesh can play an important role in increasing numerical efficiency. Another potential advantage is the flexibility in implementing different basis functions. For example, for the CDFT case, a Gaussian basis may yield better convergence and further reduction in the degree of freedom. Such an approach has been applied to quantum density functional theory calculations [66]. Lastly, the real-space formulation also allows for the development of multi-scale techniques such as the quasicontinuum reduction of field theories [67, 68] (proposed originally in the context of electronic structure calculations [67]), which can potentially enable large-scale CDFT and PFC simulations.

IX. SUMMARY AND DISCUSSIONS

We proposed a rational function fit (RFF) to describe the two-body DCF in Fourier space in order to alleviate the computational demand of the CDFT and enhance the predictive capability of the PFC method.

- We used the RFFs to show that the short-wavelength contributions of the two-body DCF play an important role in determining the thermodynamic properties of materials. Our studies demonstrate that an inaccurate representation of the correlations in the two-body DCF in favor of more computationally efficient density profiles may result in inaccurate predictions. In particular, we find that the correlations up to the third peak of the Fe DCF are important.

- We showed that it is possible to empirically parameterize the two-body DCF such that most of the predicted thermodynamic properties are in agreement with the CDFT simulation using the full two-body DCF without incurring significant computational costs.

- A combined RFF and polynomial fit was shown to provide an improved representation

of the two-body DCF in the PFC method.

- The RFF method allows the convolution integral to be numerically evaluated in real space by solving a set of inhomogeneous Helmholtz equations. Such a real-space formulation enables descriptions of nonperiodic systems and the use of non-uniform/adaptive grids.

We note that another method of constructing the two-body DCF in Fourier space was recently proposed using Gaussian peaks and was applied to the PFC method to study phase transformations [69, 70]. The use of Gaussian functions is a convenient choice for constructing a kernel corresponding to the DCF that results in various stable equilibrium crystal structures because it allows one to control the location and the width of the peaks precisely. However, the RFF is an appropriate choice when the two-body DCF obtained from experiments or MD simulations needs to be accurately described; it is difficult to use the Gaussian function to describe the oscillatory behavior of two-body DCFs. Furthermore, the RFF allows for a real-space formulation via the solution of Helmholtz equations, and provides the framework for development of multiscale methods, which is a topic for future investigation.

X. ACKNOWLEDGEMENTS

This research was supported by National Science Foundation under grant No. DMR-1105409, grant No. 0746424, and the Thai Scholar fellowship.

Appendix A: GAUSSIAN APPROXIMATION OF DENSITY PROFILES

We present a method to construct an approximate density profile using a Gaussian function. We assume that the atomic probability density around each lattice site located at $\mathbf{R}_i$ is represented by a Gaussian function of the form:

$$G(\mathbf{r}, \mathbf{R}_i) = \left(\frac{\alpha_g}{\pi}\right)^{3/2} \exp\left(-\alpha_g |\mathbf{r} - \mathbf{R}_i|^2\right), \tag{A1}$$

where the parameter α_g controls the peak width. We can construct the approximate density profile, $\rho_g(\mathbf{r})$, with an average density of ρ from a summation of the individual Gaussian

peaks:

$$\rho_g(\mathbf{r}) = \frac{\rho}{G_{avg}} \sum_i G(\mathbf{r}, \mathbf{R}_i), \tag{A2}$$

where

$$G_{ave} = \frac{1}{V} \int_V \sum_i G(\mathbf{r}, \mathbf{R}_i) d\mathbf{r}. \tag{A3}$$

The semi-analytical method utilized in this work minimizes the free energy as a function of ρ with respect to α_g and the lattice spacing.

---

[1] H. Van Swygenhoven, Materials Science and Engineering: A **483-484**, 33 (2008).

[2] D. Fan and L.-Q. Chen, Acta Materialia **45**, 611 (1997).

[3] L. Granasy, T. Pusztai, T. Börzsönyi, J. A. Warren, and J. F. Douglas, Nature Materials **3**, 645 (2004).

[4] A. Kazaryan, Y. Wang, S. Dregia, and B. Patton, Acta Materialia **50**, 2491 (2002).

[5] S. G. Kim, D. I. Kim, W. T. Kim, and Y. B. Park, Physical Review E **74**, 061605 (2006).

[6] J. A. Warren, R. Kobayashi, A. E. Lobkovsky, and W. C. Carter, Acta Materialia **51**, 6035 (2003).

[7] J. Heulens and N. Moelans, Scripta Materialia **62**, 827 (2010).

[8] R. Kobayashi, J. A. Warren, and W. C. Carter, Physica D-Nonlinear Phenomena **119**, 415 (1998).

[9] R. Kobayashi, J. A. Warren, and W. C. Carter, Physica D-Nonlinear Phenomena **140**, 141 (2000).

[10] N. Moelans, B. Blanpain, and P. Wollants, Physical Review B **78**, 024113 (2008).

[11] N. Moelans, B. Blanpain, and P. Wollants, Physical Review Letters **101**, 025502 (2008).

[12] B. Morin, K. R. Elder, M. Sutton, and M. Grant, Physical Review Letters **75**, 2156 (1995).

[13] Y. Jin and A. Khachaturyan, Philosophical Magazine Letters **81**, 607 (2001).

[14] D. Rodney, Y. Le Bouar, and A. Finel, Acta Materialia **51**, 17 (2003).

[15] Y. Wang, Y. Jin, A. Cuitino, and A. Khachaturyan, Acta Materialia **49**, 1847 (2001).

[16] Y. Wang and J. Li, Acta Materialia **58**, 1212 (2010).

[17] R. Evans, Advances in Physics **28**, 143 (1979).

[18] R. Evans, Fundamentals of Inhomogeneous Fluids (New York: Dekker, 1992).

[19] Y. Singh, Physics Letters pp. 1–94 (1991).

[20] K. R. Elder, M. Katakowski, M. Haataja, and M. Grant, Physical Review Letters **88**, 245701 (2002).

[21] K. R. Elder and M. Grant, Physical Review E **70**, 051605 (2004).

[22] N. Provatas, J. A. Dantzig, B. Athreya, P. Chan, P. Stefanovic, N. Goldenfeld, and K. R. Elder, Journal of the Minerals, Metals and Materials Society **59**, 83 (2007).

[23] T. V. Ramakrishnan and M. Yussouff, Physical Review B **19**, 2775 (1979).

[24] T. Ramakrishnan, Pramana **22**, 365 (1984).

[25] A. Archer and R. Evans, Journal of Chemical Physics **121**, 4246 (2004).

[26] U. Marconi and P. Tarazona, Journal of Physics: Condensed Matter **12**, A413 (2000).

[27] U. Marconi and P. Tarazona, Journal of Chemical Physics **110**, 8032 (1999).

[28] J. Swift and P. Hohenherg, Physical Review A **15**, 319 (1977).

[29] K. R. Elder, N. Provatas, J. Berry, P. Stefanovic, and M. Grant, Physical Review B **75**, 064107 (2007).

[30] A. Jaatinen, C. V. Achim, K. R. Elder, and T. Ala-Nissila, Physical Review E **80**, 031602 (2009).

[31] N. Pisutha-Arnond, V. W. L. Chan, K. R. Elder, and K. Thornton, Physical Review B (in press).

[32] D. C. Wallace, Solid State Physics, vol. 25 (Academic Press, New York and London, 1970).

[33] D. C. Wallace, Thermodynamics of Crystals (Dover Publications, Inc., Mineola, New York, 1998).

[34] D. C. Wallace, Physical Review **162**, 776 (1967).

[35] P. Stefanovic, M. Haataja, and N. Provatas, Physical Review Letters **96**, 225504 (2006).

[36] P. Stefanovic, M. Haataja, and N. Provatas, Physical Review E **80**, 046107 (2009).

[37] K. A. Wu and A. Karma, Physical Review B **76**, 184107 (2007).

[38] K. A. Wu, (private communication).

[39] K. A. Wu, A. Karma, J. J. Hoyt, and M. Asta, Physical Review B **73**, 094101 (2006).

[40] J. Mellenthin, A. Karma, and M. Plapp, Physical Review B **78**, 184110 (2008).

[41] Note1, in Ref. [30], the solid free energy curve is obtained by minimizing the free energy density with respect to the lattice spacing for a prescribed solid average-density. However, we

find that the evaluation of the energy-minimizing lattice spacing for each prescribed density is not necessary because the energy-minimizing lattice spacing is only weakly dependent on the average density. In particular, we find that, by using $\hat{C}^{(2)}_{MD}(k)$, the energy-minimizing lattice spacing over the range of $(\rho-\rho_0)/\rho_0$ from 0.1 to 0.3 only varies by 0.01%. The error introduced to the energy density by using the same lattice spacing for the density range of interest is only on the order of 0.1%. Therefore, we only calculate the energy-minimizing lattice spacing once for each free energy curve, making the evaluation process significantly faster.

[42] K. A. Wu, A. Adland, and A. Karma, Physical Review E **81**, 061601 (2010).

[43] L. N. Trefethen and D. I. Bau, Numerical Lineaer Algebra (SIAM, Philadelphia, 1997).

[44] A. Greenbaum, Iterative Methods for Solving Linear Systems (SIAM, Philadelphia, 1997).

[45] H. A. van der Vorst, Iterative Krylov methods for large linear systems (Cambridge University Press, New York, 2003).

[46] D. M. Young, Iterative Solution of Large Linear Systems (Academic Press, Inc., 1971).

[47] P. R. Amestoy, I. S. Duff, J. Koster, and J.-Y. L'Excellent, SIAM Journal on Matrix Analysis and Applications **23**, 15 (2001).

[48] P. R. Amestoy, A. Guermouche, J.-Y. L'Excellent, and S. Pralet, Parallel Computing **32**, 136 (2006).

[49] O. Schenk and K. Gärtner, Electronic Transactions on Numerical Analysis **23**, 158 (2006).

[50] O. Schenk and K. Gärtner, Future Generation Computer Systems **20**, 475 (2004).

[51] X. Li and J. W. Demmel, ACM Transactions on Mathematical Software **29**, 110 (2003).

[52] Y. A. Erlangga, Archives of Computational Methods in Engineering **15**, 37 (2008).

[53] O. G. Ernst and M. J. Gander, Numerical Analysis of Multiscale Problems **83**, 325 (2012).

[54] G. Hadley, Journal of Computational Physics **203**, 358 (2005).

[55] Note2, for a set of coefficients (α_i, A_j) where the real part of α_j is positive, the discretization matrix of the Helmholtz equation is not indefinite.

[56] Y. Saad and M. H. Schultz, Siam Journal on Scientific and Statistical Computing **7**, 856 (1986).

[57] M. Frigo and S. G. Johnson, Proceedings of the IEEE **93**, 216 (2005).

[58] S. Filippone, The IBM parallel engineering and scientific subroutine library (Springer Berlin Heidelberg, 1995).

[59] D. Pekurovsky, Siam Journal on Scientific Computing **34**, C192 (2012).

[60] Note3, the reported time for the CIJ/SIJ method is obtained by using an initial condition that is slightly perturbed from the solution to the Helmholtz equation. The amount of perturbation is equivalent to evolving the system using Eq. (18) where the time step is set to 10^{-5}. The calculation time using the CIJ/SIJ method can be further reduced by choosing an initial condition that is perturbed even less from the solution. For example, using a perturbation equivalent to the time step of 10^{-8}, the calculation time reduces to 0.02 s. However, during evolution, the speedup factor per iteration ($3.4/0.02 = 170$) is much less than the factor of increase in the number of iterations ($10^{-5}/10^{-8} = 1000$). Therefore, to optimize the total simulation time, both calculation time per iteration and the number of iterations need to be considered.

[61] M. Cheng and J. A. Warren, Journal of Computational Physics **227**, 6241 (2008).

[62] H. Gomez and X. Nogueira, Computer Methods in Applied Mechanics and Engineering **249-252**, 52 (2012).

[63] Z. Hu, S. M. Wise, C. Wang, and J. S. Lowengrub, Journal of Computational Physics **228**, 5323 (2009).

[64] G. Tegze, G. Bansel, G. I. Tóth, T. Pusztai, Z. Fan, and L. Gránásy, Journal of Computational Physics **228**, 1612 (2009).

[65] C. Wang and S. M. Wise, Siam Journal on Numerical Analysis **49**, 945 (2011).

[66] S. Yamakawa and S.-A. Hyodo, Physical Review B **71**, 035113 (2005).

[67] V. Gavini, K. Bhattacharya, and M. Ortiz, Journal of the Mechanics and Physics of Solids **55**, 697 (2007).

[68] M. Iyer and V. Gavini, Journal of the Mechanics and Physics of Solids **59**, 1506 (2011).

[69] M. Greenwood, N. Provatas, and J. Rottler, Physical Review Letters **105**, 045702 (2010).

[70] M. Greenwood, J. Rottler, and N. Provatas, Physical Review E **83**, 031601 (2011).

Quantity	8P	3R2P
$\hat{C}^{(2)}(0)$	-49.0	-49.0
k_m	2.99	2.98
$d^2/dk^2\left[\hat{C}^{(2)}(k_m)\right]$	-10.4	-10.4

TABLE I. Comparison of the long-wavelength limit, $\hat{C}^{(2)}(0)$, location, k_m, and curvature, $d^2/dk^2\left[\hat{C}^{(2)}(k_m)\right]$, of the first peak of from the 8P and the 3R2P fit.

Quantity	$\hat{C}^{(2)}_{MD}$ CDFT	9R CDFT	7R CDFT	5R CDFT	3R CDFT	8P CDFT
Liquid-coexistent density (Å^{-3})	0.0877	0.0896	0.0909	0.0923	0.109	0.109
(% Difference from $\hat{C}^{(2)}_{MD}$ CDFT)		(2.1%)	(3.6%)	(5.2%)	(24%)	(24%)
Solid-coexistent density (Å^{-3})	0.0902	0.0918	0.0930	0.0940	0.110	0.109
(% Difference from $\hat{C}^{(2)}_{MD}$ CDFT)		(1.9%)	(3.1%)	(4.3%)	(22%)	(21%)
Expansion in melting (Å^3/atom)	0.304	0.271	0.249	0.198	0.0373	0.0211
γ_{100} (erg/cm^2)	88.7	84.3	81.3	67.4	13.7	6.53
γ_{110} (erg/cm^2)	86.6	81.9	79.0	65.5	13.5	6.37
FCC crystal	S	S	S	MS	NS	NS

TABLE II. The comparison of the liquid and solid properties computed from the CDFT simulations using different fits of the EAM-MD data, $\hat{C}^{(2)}_{MD}(k)$. The abbreviations S, MS, and NS denote "stable", "metastable", and "not stable", respectively (see text). The data are rounded to three significant digits.

Quantity	$\hat{C}^{(2)}_{MD}$ CDFT	M5R CDFT	9R CDFT	5R CDFT
Liquid-coexistent density (Å^{-3})	0.0877	0.0879	0.0896	0.0923
(% Difference from $\hat{C}^{(2)}_{MD}$ CDFT)		(0.19%)	(2.1%)	(5.2%)
Solid-coexistent density (Å^{-3})	0.0902	0.0901	0.0918	0.0940
(% Difference from $\hat{C}^{(2)}_{MD}$ CDFT)		-- [a]	(1.9%)	(4.3%)
Expansion in melting (Å^3/atom)	0.304	0.279	0.271	0.198
γ_{100} (erg/cm^2)	88.7	86.5	84.3	67.4
γ_{110} (erg/cm^2)	86.6	83.9	81.9	65.5
FCC crystal	S	MS	S	MS

[a] The difference is less than the uncertainty of the calculations.

TABLE III. The liquid and solid properties computed from the M5R CDFT simulations, along with the 5R and 9R CDFT simulation results from Table II.

	8P		3R2P	
$\Delta\tau$	V_w (%)	V_n (%)	V_w (%)	V_n (%)
10^{-1}	60	32	60	33
10^{-2}	3.2	3.7	3.2	3.8
10^{-3}	3.1×10^{-1}	3.6×10^{-1}	2.9×10^{-1}	3.4×10^{-1}
10^{-4}	2.9×10^{-2}	3.4×10^{-2}	2.5×10^{-2}	2.9×10^{-2}
10^{-5}	2.7×10^{-3}	3.0×10^{-3}	2.3×10^{-3}	2.7×10^{-3}
10^{-6}	7.4×10^{-4}	2.6×10^{-4}	2.1×10^{-4}	2.4×10^{-4}

TABLE IV. The comparison of the convergence values at different time step sizes using the backward Euler time stepping scheme. These values are evaluated at $\tau = 0.2$.

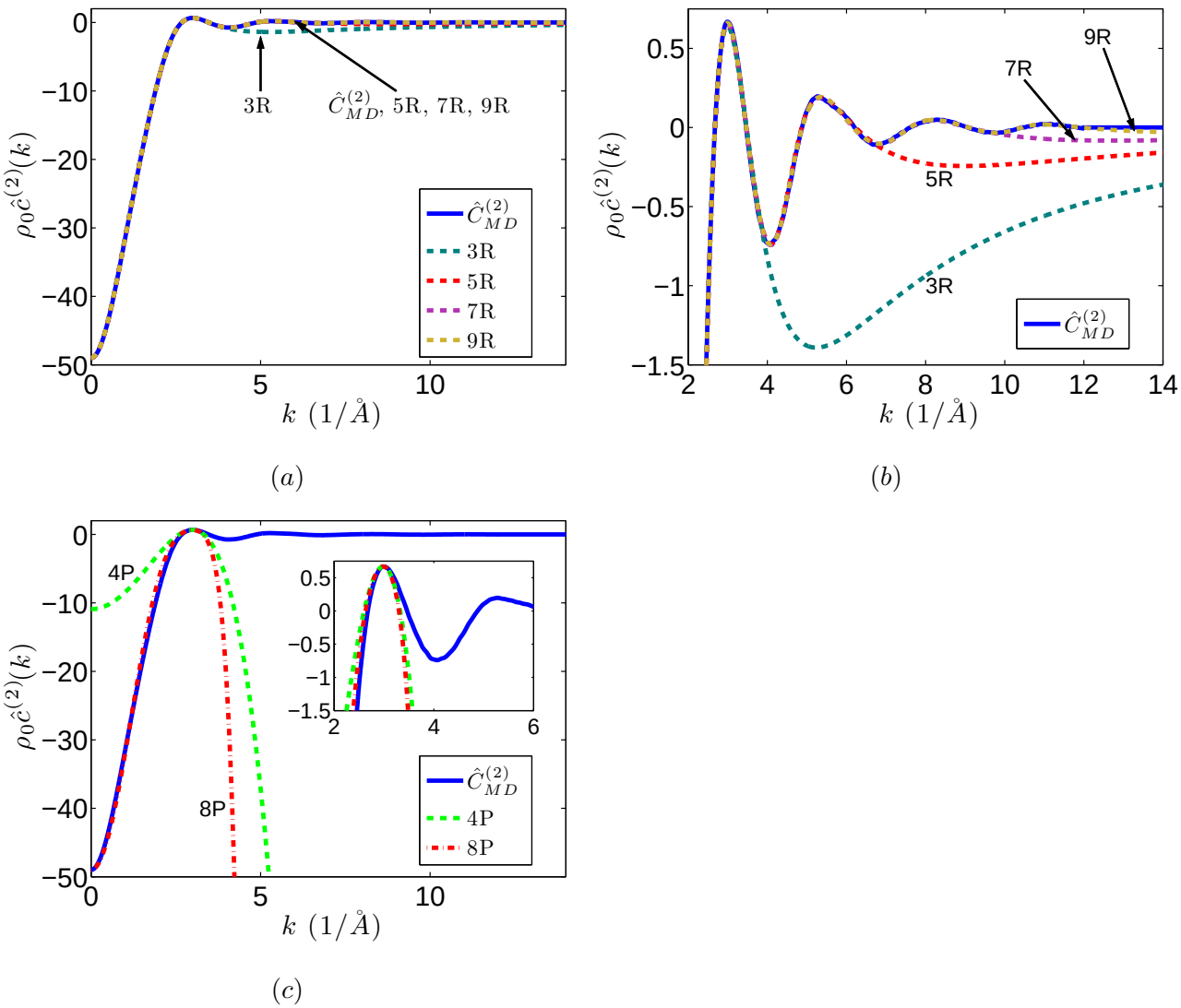

FIG. 1. (Color online) The different fits to the embedded-atom-method molecular dynamics (EAM-MD) data, $\hat{C}^{(2)}_{MD}$ [38]. (a) The rational function fits (RFFs) with different number of terms. (b) A magnified section of (a). (c) The fourth-order fit (4P) and the eighth-order fit (8P) [30, 37].

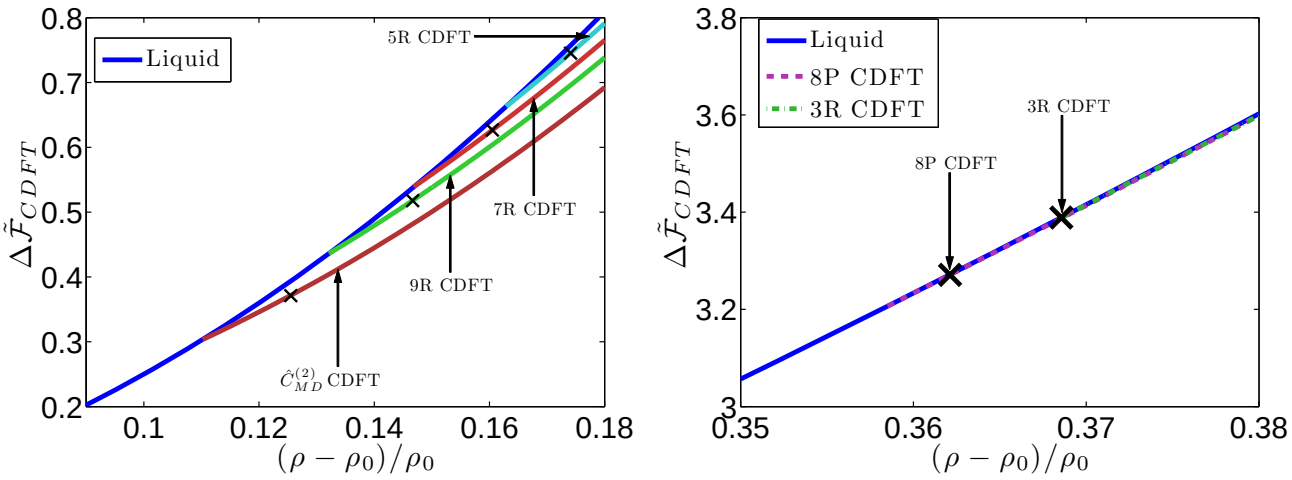

FIG. 2. (Color online) The normalized free energies per unit volume of the BCC solid corresponding to different fits of the EAM-MD data. The blue-solid line denotes the liquid free energy density curve. (a) Free energies of the BCC solid from the CDFT simulations using the EAM-MD data, 9R, 7R and 5R. The cross signs at the solid curves denote the solid densities at the solid-liquid coexistence. (b) Free energies of the BCC solid from the CDFT simulations using the 8P and 3R. The two cross signs show the solid densities at the solid-liquid coexistence.

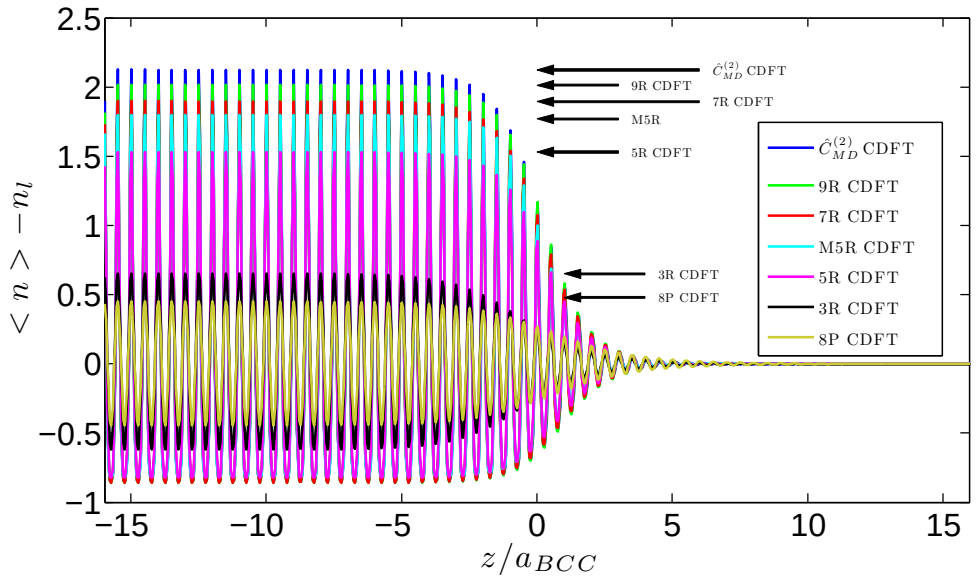

FIG. 3. (Color) The BCC solid-liquid density profiles along the direction normal to the (110) plane (z-axis), where a_{BCC} is the lattice spacing. Here, $\langle n \rangle = A^{-1} \int \int n(x, y, z) dx dy$, where A is the surface area and n_l is the normalized liquid density at the solid-liquid coexistence. The arrows indicate the amplitude of the fluctuation in the bulk solid region of the density profiles.

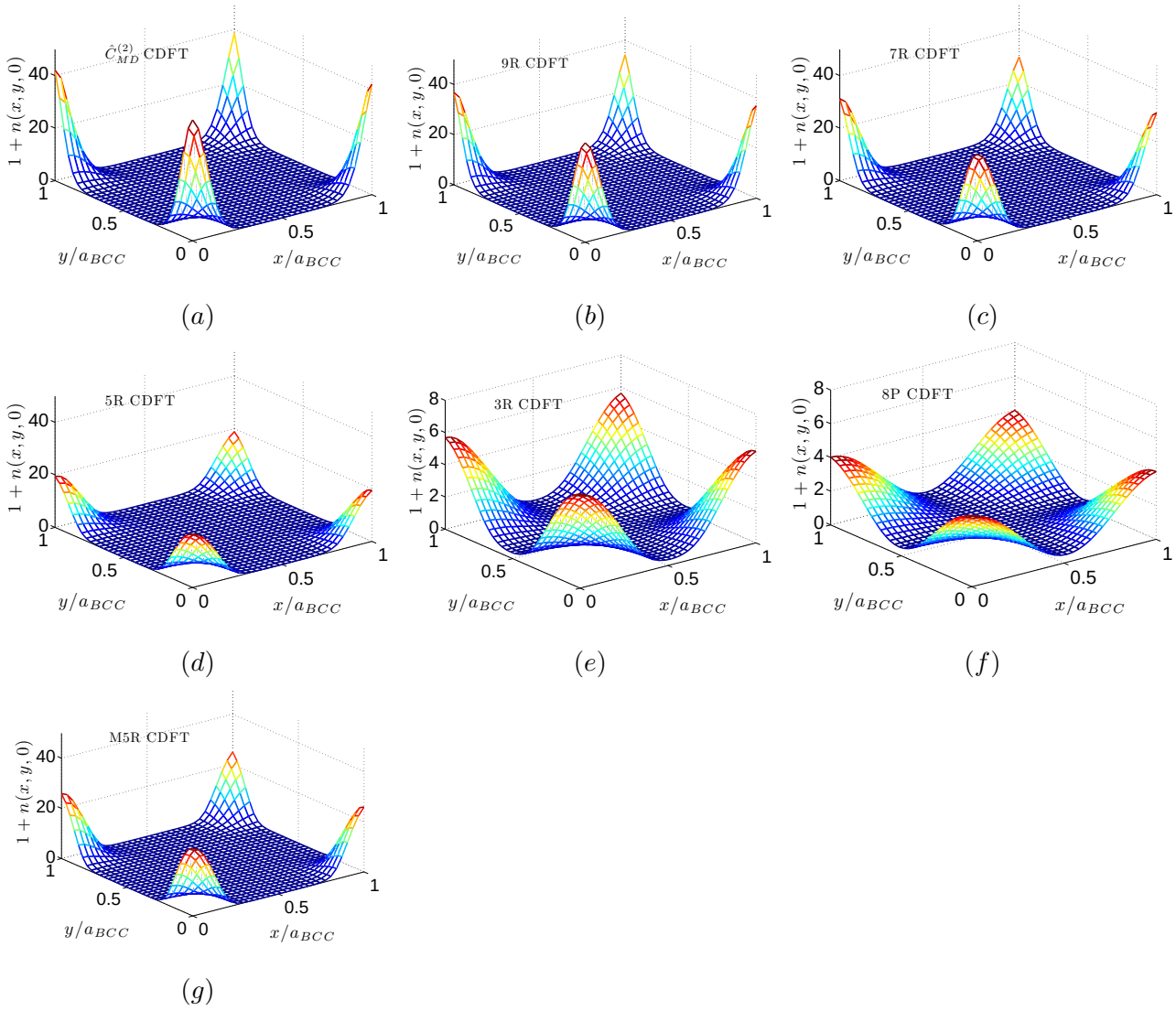

FIG. 4. (Color online) The density profiles on the (100) crystal plane of the BCC solids at the solid-liquid coexistence, where a_{BCC} is the lattice spacing. It should be noted that the vertical scales of (e) and (f) are different from the others.

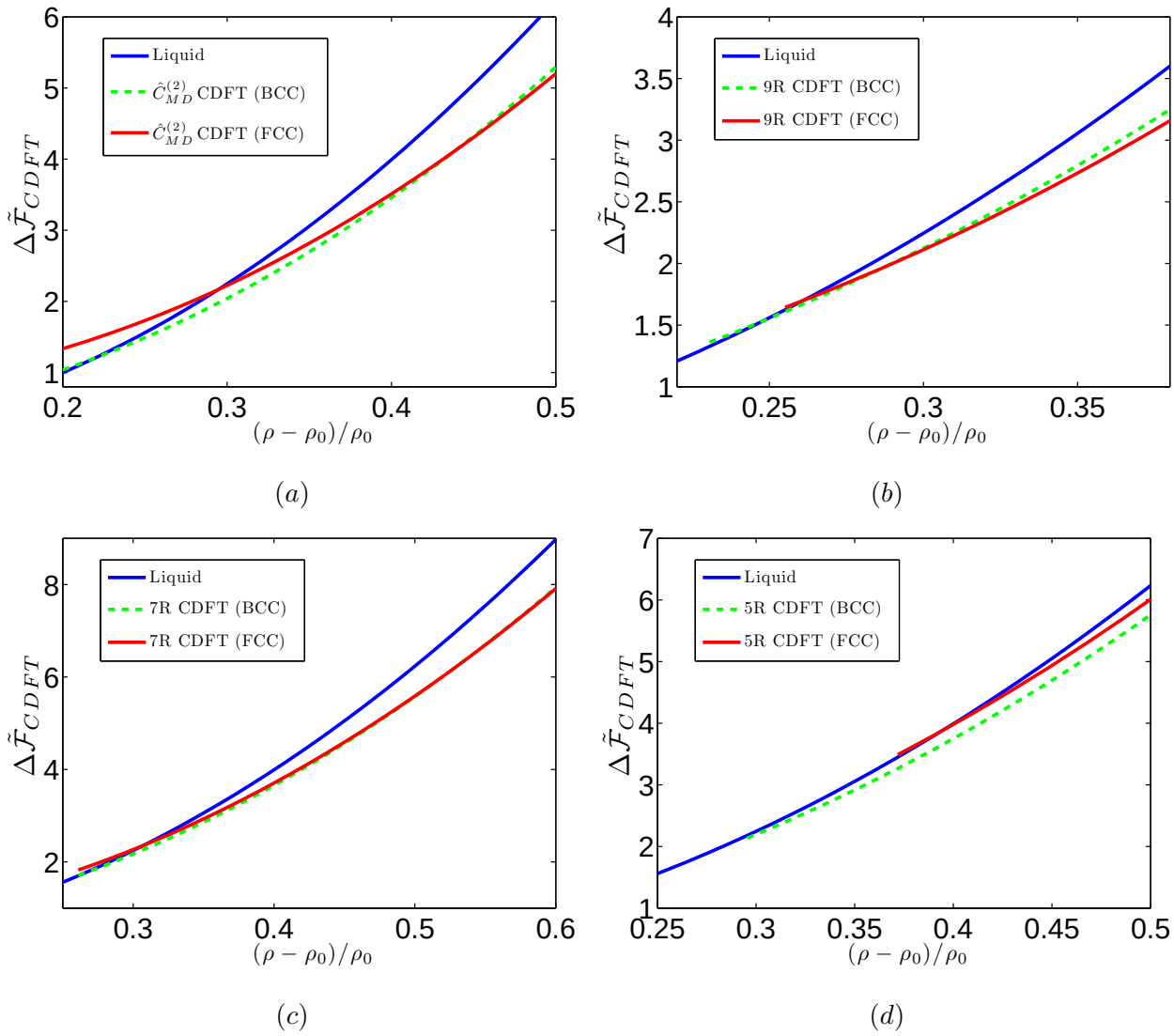

FIG. 5. (Color online) The normalized free energies per unit volume of the BCC and FCC solids from the CDFT simulations using the EAM-MD data, 9R, 7R, and 5R. The 5R-BCC and 5R-FCC curves do not intersect. The solid free energies are evaluated from the semi-analytical method described in Section IV B. The blue solid curves denote the liquid free energy.

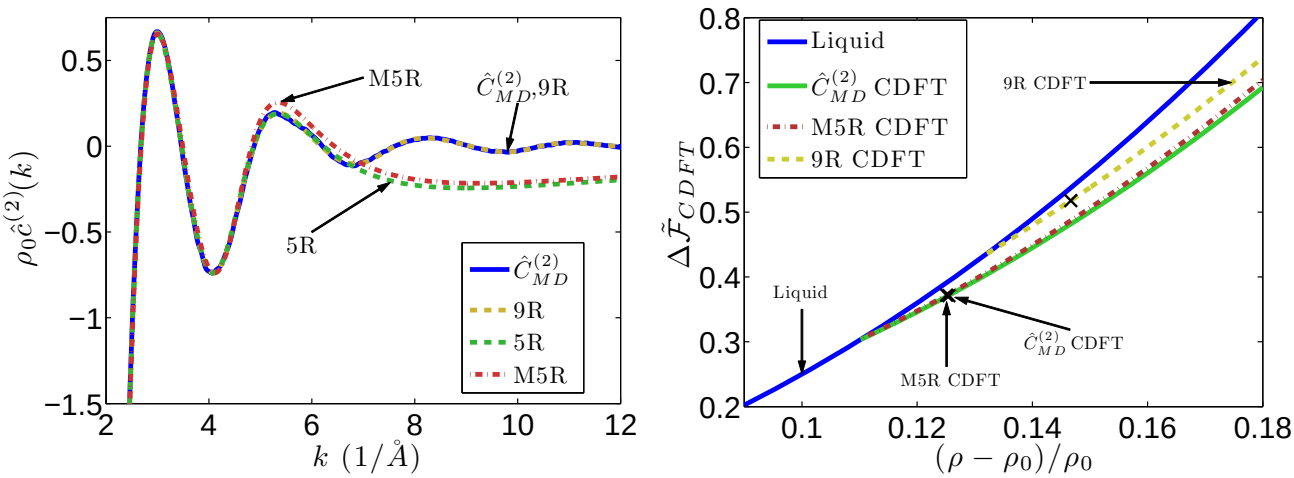

FIG. 6. (Color online) (a) The comparison between the 5R and M5R. The two fits are similar except for the second peak of the M5R being slightly higher. The solid line denotes the EAM-MD data. (b) The comparison between the normalized BCC solid free energy density from the CDFT simulations using the EAM-MD data, 9R, and M5R. The cross signs indicate the solid-coexistent densities. The cross signs on the M5R and EAM-MD free energy curves nearly coincide at the current graphical scale.

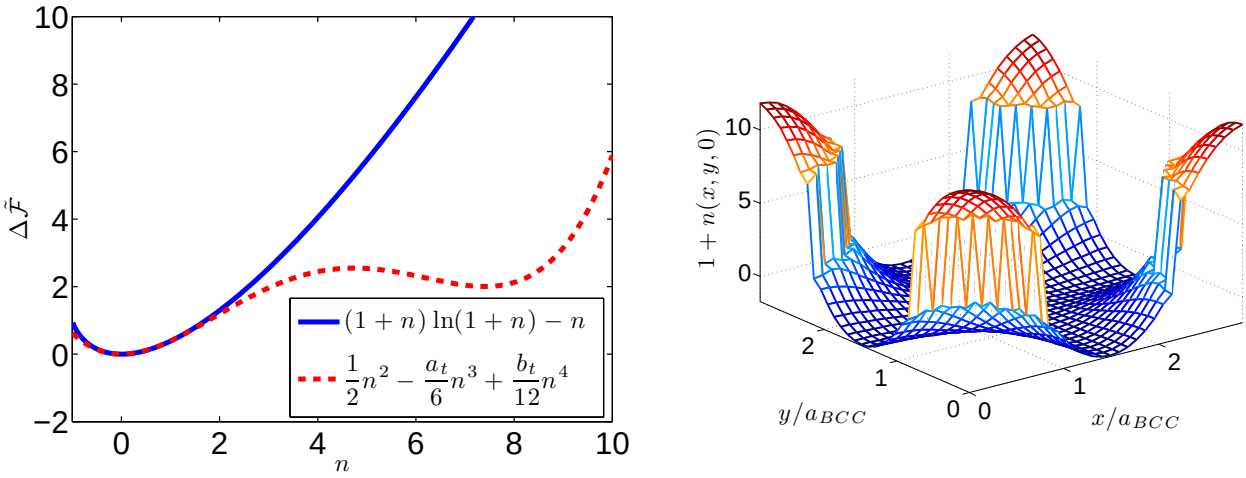

(a) (b)

FIG. 7. (Color online) The ideal contribution to the free energy as a function of the normalized density. The solid line denotes the ideal contribution from Eq. (8) while the dash line denotes the approximation from Eq. (10), where $a_t = 0.6917$ and $b_t = 0.0854$ [30]. (b) The density profile on the (100) crystal plane of the BCC solid from the simulation using the 3R and the ideal contribution represented by the dash line in (a).

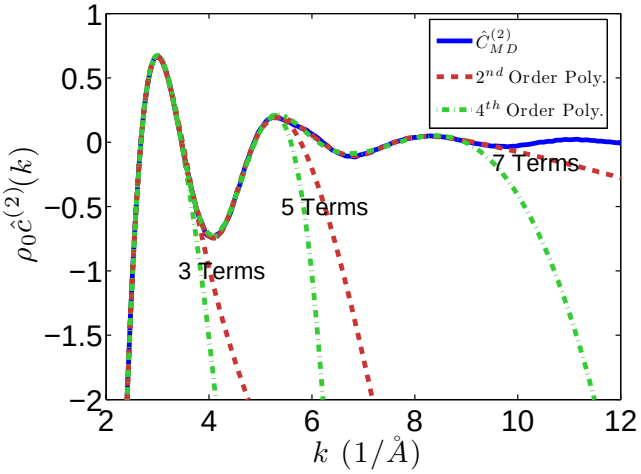

FIG. 8. (Color online) The different fits to the EAM-MD data (solid line) using the combined rational and polynomial functions. From the label, "2^{nd} Order Poly." denotes the fits that include up to k^2 in Fourier space and "4^{th} Order Poly." denotes those including k^2 and k^4 terms. The label "Terms" refers to the number of partial fraction terms in Eq. (19).

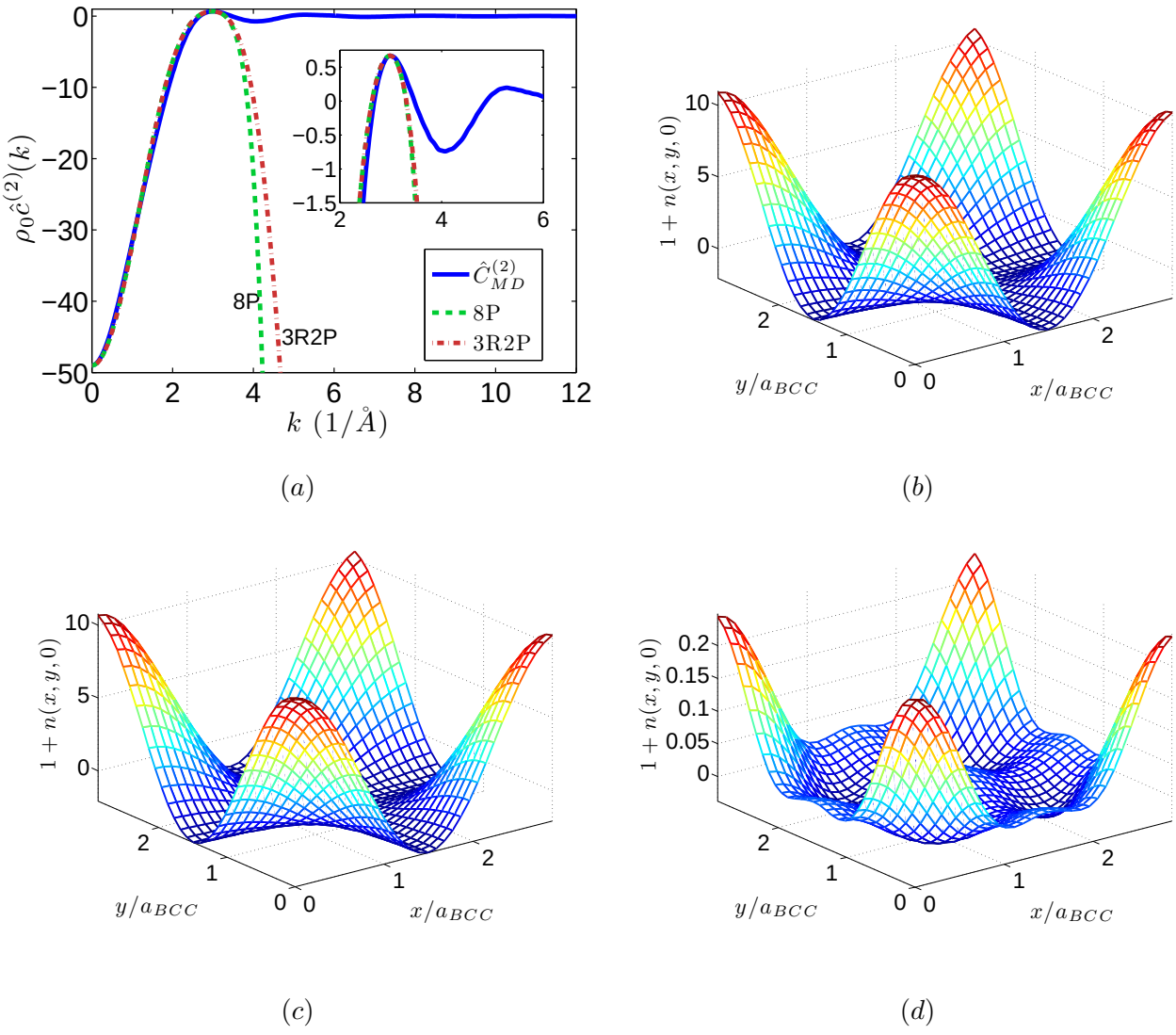

FIG. 9. (Color online) (a) The comparison between the 8P and the 3R2P. The solid line denotes the EAM-MD data. (b)-(c) The density profiles on the (100) crystal plane of the BCC solid at the solid-liquid coexistence from the PFC simulations using the 3R2P (b) and the 8P (c). (d) The difference between the density profiles of the 3R2P and 8P PFC simulations, where the profile of 8P PFC is subtracted from that of 3R2P PFC.

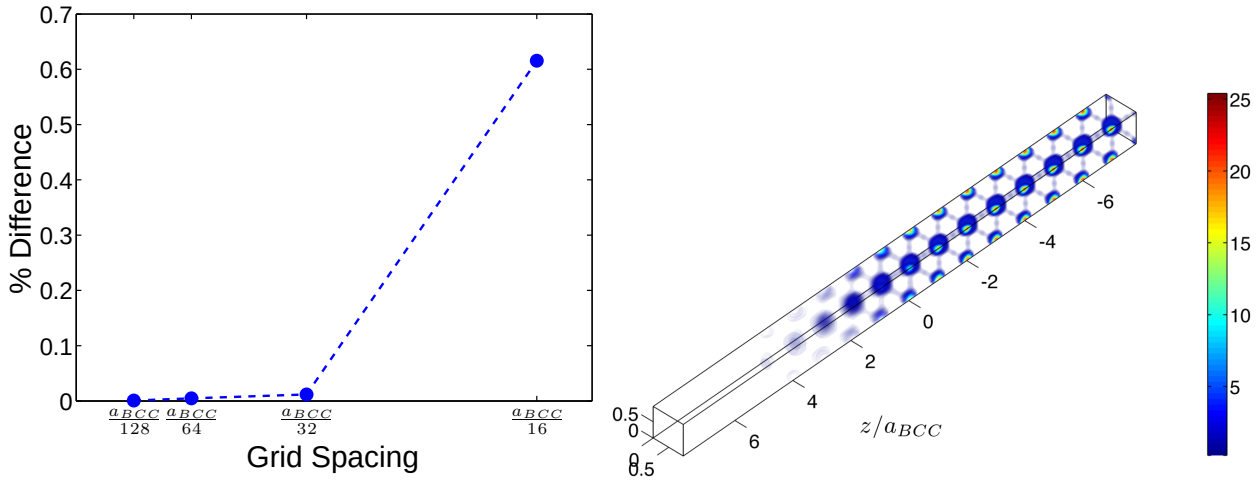

(a) (b)

FIG. 10. (Color online) (a) The difference between the solid free energy densities calculated from the M5R CDFT simulations using the CIJ/SIJ method and the numerically converged reference value. The reference value is calculated from the M5R CDFT simulation using the Fourier spectral method at a fine grid spacing of $\Delta h = a_{BCC}/256$. (b) The plot of $n(\mathbf{r})$ showing the interface between liquid and BCC solid from the M5R CDFT simulation using the CIJ/SIJ method.